RAA 2018 Vol. **18** No. **11**, 134(14pp) doi: 10.1088/1674–4527/18/11/134

http://www.raa-journal.org *http://iopscience.iop.org/raa*

***R**esearch in*
***A**stronomy and*
***A**strophysics*

SMA molecular line survey towards the massive star-forming region G10.6−0.4 in W31 complex

Wai-Ho Wong[1,2] and Tao An[1]

[1] Key Laboratory of Radio Astronomy, Shanghai Astronomical Observatory, Chinese Academy of Sciences, Shanghai 200030, China; *huangweihao@shao.ac.cn, antao@shao.ac.cn*

[2] University of Chinese Academy of Sciences, Beijing 100049, China

Received 2018 January 8; accepted 2018 May 22

Abstract Line surveys of complex molecules with millimeter and sub-millimeter telescopes are important for probing the physical and chemical environments of massive star forming regions (MSFRs). We present a molecular line survey with the Submillimeter Array (SMA) in the frequency ranges of 220.3–222.3 GHz and 230.3–232.3 GHz toward G10.6−0.4, the brightest star forming core in the W31 complex. Ninety-nine transitions from 22 molecular species and their isotopologues are identified. The moment 0 images of typical molecules show a compact core which is concentrated at the continuum peak position. Based on the local thermodynamic equilibrium assumption, the molecular line data are modeled. The rotational temperatures of those molecular species range from 96 to 178 K and their column densities range from 2.0×10^{14} to 3.7×10^{17} cm^{-2}. The observational data suggest that all complex molecules are located in a warm environment. Chemical environments of the molecules are discussed. We compared molecular abundances and gas temperatures in G10.6−0.4 with those in other MSFRs, and found that gas temperatures and fractional abundances of specific molecules in G10.6−0.4 are similar to the typical MSFR W51 North, suggesting that there are similar physical and chemical environments in these two MSFRs.

Key words: stars: formation — ISM: abundances — ISM: individual objects: G10.6−0.4 — ISM: molecules — radio lines: ISM

1 INTRODUCTION

The formation of massive stars is one of the frontier topics in modern astrophysics. Due to the high dust extinction and complex dynamic environment, and also because high-mass stars are short-lived compared with low-mass ones, the early evolution of massive star forming regions (MSFRs) is not well understood yet (see reviews in Zinnecker & Yorke 2007).

G10.6−0.4 is the most compact far-infrared source in the W31 complex (Wright et al. 1977), and it is associated with the brightest radio continuum source in this region (Goss & Shaver 1970). OH and H_2O masers were detected in the ultra compact HII region G10.6−0.4 (Turner & Rubin 1971; Habing et al. 1974; Fish et al. 2005), suggesting on-going massive star formation activities in this region (Ho & Haschick 1981; Keto et al. 1988). The VLA observations of NH_3 have revealed evidence of a collapsing molecular core toward the central OB cluster (Ho & Haschick 1986). Both gas infalling (e.g., Sollins et al. 2005) and energetic molecular outflow (e.g., Liu et al. 2010) have been detected in this source. All the evidence suggests G10.6−0.4 could be in an early stage of stellar evolution. The kinematic distance of this source was determined as ∼6 kpc from absorption lines toward the HII regions, such as using 21 cm hydrogen absorption lines (Caswell et al. 1975), H_2CO and OH absorption lines (Wilson 1974), and H110α and H_2CO (Downes et al. 1980). At this distance, the inferred infrared luminosity is about $10^6\,L_\odot$. However, the accuracy of these kinematic distance measurements is affected by the compli-

cated distribution of numerous gas clouds along the line of sight. A recent trigonometric parallax measurement with observations of water and methanol masers yielded a more accurate distance of $4.95^{+0.51}_{-0.43}$ kpc (Sanna et al. 2014), placing the complex $\sim 20\%$ closer than the previous estimate. Nevertheless, G10.6−0.4 is still one of the most luminous HII regions with embedded OB stars and thus is a good template for investigating massive star formation.

The physical and chemical environments in molecular clouds play the key role of controlling the star formation process (e.g., van Dishoeck & Blake 1998; Evans 1999). At present, the kinematics and dynamics of G10.6−0.4 have been well studied as mentioned above, while the physical and chemical characteristics of the molecular gas have not been investigated in detail. Emission lines of complex organic molecules offer useful clues for probing the physical conditions (density and temperature), gas kinematics and excitation conditions in MSFRs (Herbst & van Dishoeck 2009). High-frequency and high-resolution line surveys with millimeter and submillimeter interferometers are especially critical for investigating compact high-excitation regions, such as the hot cores of molecular clouds. Thanks to the broad bandwidth (a total of 4 GHz) of the Submillimeter Array (SMA), multiple complex molecules can be observed simultaneously in the line survey, allowing for studying the physical and chemical properties of the SFRs in a consistent way.

In this paper, we present line survey results derived from the SMA observations of G10.6−0.4. The present paper will concentrate on the physical and chemical condition of the molecular gas in the hot core. Section 2 describes the observations and data reduction. Section 3 presents the continuum emission, line identification and gas distribution. The temperatures and column densities of the molecular gas in its hot core are calculated by using XCLASS[1] and MAGIX[2] software packages. Properties of nitrogen-bearing, oxygen-bearing and sulfur-bearing molecular species, and the methyl acetylene molecule are discussed in Section 4. By comparing the rotational temperatures and fractional abundances of different hot cores in the Milky Way, we speculate on the evolution stages of G10.6−0.4. Section 5 summarizes this work.

[1] *https://xclass.astro.uni-koeln.de/*

[2] *https://magix.astro.uni-koeln.de/*

2 OBSERVATIONS AND DATA REDUCTION

The observations of G10.6−0.4 used in this paper were carried out with the SMA (Ho et al. 2004) at the 230 GHz band on 2009 January 31. Eight antennas participated in the observation in the compact array configuration. However the antenna with the longest baseline failed to create useful data, resulting in a reduction in the maximum baseline length to 69 m, corresponding to the highest resolution of about $2.5''$. The phase-tracking center is at $\mathrm{RA} = 18^{\mathrm{h}}10^{\mathrm{m}}28.698^{\mathrm{s}}$, $\mathrm{Dec} = -19°55' 48.68''$ (J2000.0), which is the same as that adopted in Liu et al. (2013) and close to the 1.3 cm free-free continuum peak revealed by Liu et al. (2011). The weather conditions during the observations were excellent with a typical system temperature of 97 K. A total of 4 GHz bandwidth is split into two discrete sidebands: the lower sideband (LSB) from 220.3−222.3 GHz and the upper sideband (USB) from 230.3−232.3 GHz. The frequency resolution is 0.406 MHz, corresponding to a velocity resolution of $\sim$0.5 km s^{-1}. The data were calibrated and imaged in the Miriad[3] software package. The bandpass responses of each telescope were calibrated using QSO 3C 454.3. QSO 1733−130 was used for phase calibration. The planet Uranus was utilized for flux density calibration of the visibility data, and we estimated an uncertainty of $\sim$10% for the absolute flux scale. Continuum emission was averaged from the line free channels in both LSB and USB and subtracted from the line data in the ultraviolet domain. Self-calibration was performed with the continuum data. The obtained gain solutions were then applied to correct the phase of the line data. The synthesized beam size of the continuum and line images is approximately $5.6'' \times 2.6''$, with $\mathrm{P.A.} = 2.1°$. 1σ root mean square (rms) noise in the continuum and line image is approximately 0.15 Jy beam^{-1} and 0.2 Jy beam^{-1} per channel, respectively.

3 RESULTS

3.1 Continuum Emission

The 1.3 mm continuum image is shown in Figure 1, which is constructed by averaging the line-free channels in the LSB and USB. The continuum emission is concentrated on the central compact core which displays an elongation along the northwest-southeast direction. The continuum peak is located at RA=$18^{\mathrm{h}}10^{\mathrm{m}}28.685^{\mathrm{s}}$ and

[3] *http://www.astro.umd.edu/∼teuben/miriad/*

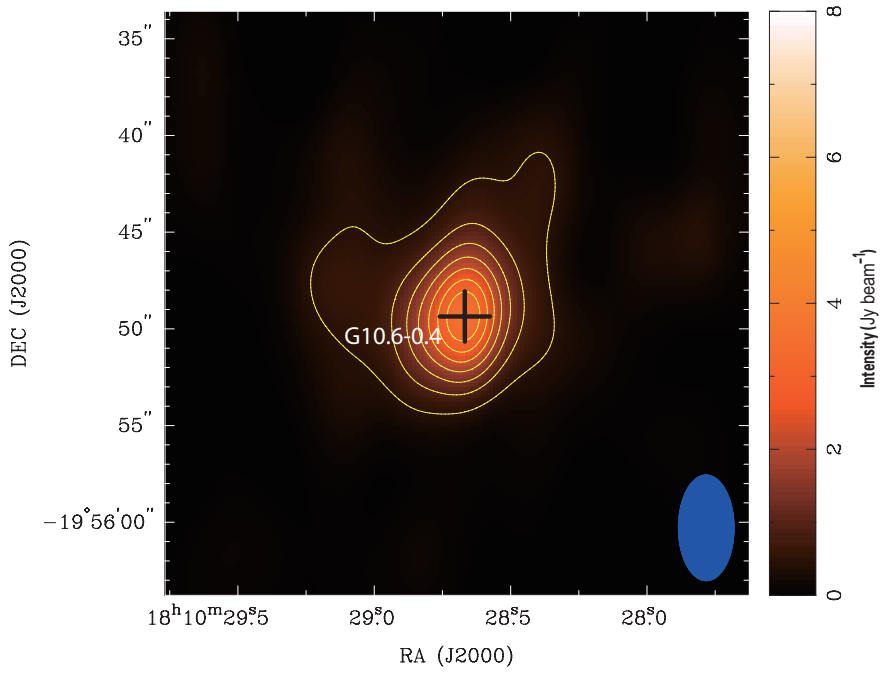

Fig. 1 1.3 mm continuum image of G10.6−0.4. The contours represent 0.5, 0.9, 1.4, 1.6, 2.3, 2.7, 3.2 and 3.6 Jy beam^{-1}. The lowest contour is about 3 times the rms noise (= 0.15 Jy beam^{-1}). The color scale shows the intensity range from 0 to 8 Jy beam^{-1}. The synthesized beam ($5.6'' \times 2.6''$, P.A. $= 2.1°$) is shown in the bottom-right corner and the *cross* indicates the peak position of continuum emission, RA $= 18^{\rm h}10^{\rm m}28.685^{\rm s}$, Dec $= -19°55'\ 49.149''$

.

Dec $= -19°56'49.149''$. The general morphology is consistent with the 1.1 mm SMA image from the compact array configuration obtained by Liu et al. (2013), but our image sensitivity is 2 times higher. Two-dimensional Gaussian fitting was applied to the central continuum source, giving the source size $\sim 5.2'' \times 3.6''$ (P.A. $= -59.7°$), as well as peak intensity $\sim 3.0 \pm 0.3$ Jy beam^{-1} and integrated flux density ∼7.4±0.7 Jy.

Figure 1 shows some extensions to the east and northwest from the central clump. Such extensions coincide with the dense cores found in figure 1 of Liu et al. (2013).

A rotational temperature of 156 K is obtained from the local thermodynamic equilibrium (LTE) calculation using the CH_3CN line (see details in Sect. 3.4). Since the 1.3 mm continuum data contain free-free emission from ionized gas and thermal emission from dust grains, we must first remove the free-free emission contribution from the 1.3 mm continuum emission before estimating H_2 column density and mass from the dust emission. We assume that the emission in the ionized hydrogen region is optically thin, and the flux density of the free-free emission ($S(\nu)$) is directly proportional to $\nu^{-0.1}$. By adopting the measured flux density of 2.5 Jy at 23 GHz (Keto et al. 1987) and the radio spectral index of −0.1, the 1.3 mm free-free emission is calculated to be 2.0 Jy. After subtracting the contribution from the free-free emission, the 1.3 mm flux density of the dust emission is thus 5.4 Jy. We assumed that the dust temperature is equal to the CH_3CN gas temperature, and adopted the grain emissivity $Q(\nu) = 2.2 \times 10^{-5}$ at frequency of 230 GHz and the grain emissivity law slope $\beta = 1.5$ (Lis et al. 1991).

According to the following two equations:

$$N_{\rm H_2} = 8.1 \times 10^{17} \frac{e^{\frac{h\nu}{kT}} - 1}{Q(\nu)\Omega} \left(\frac{S_\nu}{\rm Jy}\right) \times \left(\frac{\nu}{\rm GHz}\right)^{-3} \ ({\rm cm}^{-2}) \quad (1)$$

and

$$M_{\rm H_2} = 1.3 \times 10^{4} \frac{e^{\frac{h\nu}{kT}} - 1}{Q(\nu)} \left(\frac{S_\nu}{\rm Jy}\right) \times \left(\frac{\nu}{\rm GHz}\right)^{-3} \left(\frac{D}{\rm kpc}\right)^{2} \ (M_\odot)\ , \quad (2)$$

the hydrogen column density $N_{\rm H_2} = (1.3 \pm 0.1) \times 10^{24}$ cm^{-2} and the total hydrogen mass $M_{\rm H_2} \sim 514.7 \pm 51.8\, M_\odot$ can be calculated using the integrated continuum flux density (Lis et al. 1991). Here, h is the Planck

constant, ν the rest frequency, k the Boltzmann constant, T dust temperature, $Q(\nu)$ grain emissivity, Ω solid angle of beam, S_ν total integrated flux density of the continuum source and D distance between the source and the Sun. The derived total $M_{\rm H_2}$ is consistent with measurements reported in literature (e.g., $M_{\rm H_2} = 240 - 1040\,M_\odot$, Liu et al. 2010). Furthermore, hydrogen mass of the interior core $M_{\rm H_2,core} \sim 208.8 \pm 20.9\,M_\odot$ is estimated from the peak intensity. This value is consistent with the central core mass $\sim 200\,M_\odot$ derived from previous studies (e.g., Keto 2002; Liu et al. 2013), suggesting that the compact central region of G10.6−0.4 contains a cluster of massive stars.

3.2 Gas Distribution

The LSB and USB beam-averaged molecular spectra were extracted from the peak position in the 1.3 mm continuum image. Molecular transitions were identified using the XCLASS software package. The spectroscopic parameters of molecular species in XCLASS were obtained from Jet Propulsion Laboratory[4] (JPL, Pickett et al. 1998) and Cologne Database for Molecular Spectroscopy[5] (CDMS, Müller et al. 2005). The spectra (black lines) along with identified lines are shown in Figure 2. Red lines indicate the fitted spectra (for model method, see details in Sect. 3.3). Ninety-nine transitions from 22 molecular species and their isotopologues were identified, including seven nitrogen-bearing molecules (CH_2CHCN, CH_3CH_2CN, HNCO, CH_3CN, $CH_3{}^{13}CN$, $CH_3CN_{v8=1}$ and $^{13}CH_3CN$), six oxygen-bearing molecules (CH_3OCH_3, CH_3OH, $^{13}CH_3OH$, CH_3OCHO, CH_2CO and t-HCOOH), six sulphur-bearing molecules (^{13}CS, SO_2, $^{33}SO_2$, $^{34}SO_2$, OCS and $O^{13}CS$), two radio recombination lines ($H30_\alpha$ and $H38_\beta$) and CH_3CCH.

The radio recombination lines $H30_\alpha$ and $H38_\beta$ manifest large line width of 75 and 54 km s^{-1}, respectively. Since the database of XCLASS does not optimize the radio recombination lines model, the $H30_\alpha$ and $H38_\beta$ line fits were not used for this analysis. Some molecules exhibit a single transition (SO_2, HNCO, ^{13}CS, CH_3OH, OCS and $O^{13}CS$), and others show multiple transitions (CH_3CN, CH_3CCH and CH_3CH_2CN). The fitted line parameters are presented in Table 1, in which columns (1)–(8) present molecule name, quantum numbers, rest frequency, line strength ($S_{ij}\,\mu^2$), upper-level energy (E_u) and peak intensity ($I_{\rm p}$), central line velocity and the full width at half maximum (FWHM) of the line profile, respectively. Molecules with the '*' symbol indicate that the different transitions are blended with each other and cannot be separated, and molecules with the '×' symbol denote that the signal-to-noise ratios of the spectra are not high enough to give satisfactory fitting.

The velocity-integrated intensity images (moment 0 maps) of typical molecular lines and radio recombination lines are displayed in Figure 3. 3σ cutoff has been used to clip the noise in each channel when creating these images. The images of all typical molecules show a compact core structure. The peak position of the continuum emission is marked by a cross. The peaks of CH_3CH_2CN, CH_3CN, CH_3OH, $CH_3CN_{v8=1}$, OCS, CH_3CCH and radio recombination lines $H38_\beta$ coincide with the continuum peak. The peaks of CH_2CHCN and SO_2 show a slight deviation to the west of the continuum peak; whereas the peaks CH_3OCH_3, CH_3OCHO and CH_2CO are slightly offset eastward from the continuum peak. Despite small positional offsets, the peaks of nitrogen-bearing molecules and oxygen-bearing molecules are mixed well in this hot core region. Future observations with higher resolution are necessary to resolve the position offsets of these two types of molecules. The co-spatial distributions of N- and O-bearing molecules suggest that the chemical environment and origins of these molecules may be similar (Remijan et al. 2004). The emission of CH_3CH_2CN, CH_2CHCN, CH_3OCH_3, CH_3OCHO, SO_2, $CH_3CN_{v8=1}$ and $H38_\beta$ is mainly concentrated in the compact core. The line emission of CH_3OH, CH_2CO and CH_3CCH shows prominent extension to the east; the line emission CH_3OCH_3 extends to the southwest; CH_3CN and OCS exhibit extension to both the southeast and northwest directions, exceeding the distribution of continuum emission, implying molecules with the same extension may have the same kinetic mechanism. In addition, the extension of CH_3CN and OCS may be caused by a hot toroid G10.6−0.4 (Liu et al. 2010). These two molecules are often used as risk/rotation tracers (Klaassen et al. 2009).

3.3 Physical and Chemical Properties of the Molecular Gas

Complex molecules generally reside in the interior region of an SFR, therefore the rotational temperature, column density and fractional abundance of the molecular

[4] *http://spec.jpl.nasa.gov/*

[5] *http://www.cdms.de/*

Table 1 The Molecular Line Parameters

Molecule	Quantum Numbers	Frequency (MHz)	$S_{ij}\mu^2$ (debye^2)	E_u (K)	I (Jy beam^{-1})	Velocity (km s^{-1})	FWHM (km s^{-1})
(1)	(2)	(3)	(4)	(5)	(6)	(7)	(8)
CH_3CN	12_8–11_8	220475.92020	221.50317	525.57267	0.6 ± 0.1	-0.1 ± 0.3	3.5 ± 0.3
	12_7–11_7	220539.41280	263.03526	418.63118	1.0 ± 0.1	-0.1 ± 0.3	5.3 ± 0.2
	12_6–11_6	220594.49230	598.07051	325.89958	2.2 ± 0.2	-0.7 ± 0.2	5.3 ± 0.1
	12_5–11_5	220641.12000	329.47733	247.39871	2.3 ± 0.1	-0.0 ± 0.2	6.1 ± 0.2
	12_4–11_4	220679.32000	354.37162	183.14629	3.3 ± 0.2	-1.3 ± 0.1	5.3 ± 0.1
	12_3–11_3	220709.08000	747.43604	133.15712	5.1 ± 0.3	-1.4 ± 0.2	5.8 ± 0.1
	12_2–11_2	220730.27000	387.60323	97.44229	4.6 ± 0.4	-1.5 ± 0.2	6.0 ± 0.2
	12_1–11_1	220742.99000	395.92314	76.01028	$*$	$*$	$*$
	12_0–11_0	220747.24000	398.70454	68.86571	$*$	$*$	$*$
$CH_3{}^{13}CN$	12_6–11_6	220485.85870	553.66136	325.87764	$\times$	$\times$	$\times$
	12_5–11_5	220532.32730	305.07931	247.37321	0.2 ± 0.1	-0.8 ± 1.3	3.7 ± 1.0
	12_4–11_4	220570.37280	328.12765	183.11812	0.2 ± 0.1	-1.6 ± 1.1	4.2 ± 0.9
	12_3–11_3	220599.97970	692.07807	133.12661	0.8 ± 0.1	-0.9 ± 0.6	9.2 ± 0.6
	12_2–11_2	220621.13620	358.89420	97.41033	$*$	$*$	$*$
	12_1–11_1	220633.83350	366.59673	75.97734	0.8 ± 0.1	-0.3 ± 0.2	4.3 ± 0.4
	12_0–11_0	220638.06650	369.17169	68.83239	$*$	$*$	$*$
$CH_3CN\ v_8 = 1$	12_1–11_1 (1)	221199.12390	340.89476	588.02233	$*$	$*$	$*$
	12_5–11_5 (−1)	221252.34990	567.31370	839.19784	0.2 ± 0.1	-1.1 ± 2.3	4.8 ± 1.7
	12_7–11_7 (1)	221265.12120	452.95459	850.37595	$*$	$*$	$*$
	12_6–11_6 (1)	221311.83490	257.41643	771.12092	0.3 ± 0.2	-1.2 ± 0.7	2.0 ± 0.6
	12_3–11_3 (−1)	221337.92820	321.79083	698.41038	0.4 ± 0.2	0.7 ± 0.5	2.3 ± 0.4
	12_5–11_5 (1)	221350.25670	283.65311	706.05222	0.4 ± 0.2	-0.2 ± 0.5	2.2 ± 0.4
	12_2–11_2 (−1)	221367.40390	667.46322	649.41392	0.6 ± 0.1	-0.1 ± 0.4	3.9 ± 0.3
	12_4–11_4 (1)	221380.59520	610.30193	655.19546	0.5 ± 0.1	-0.1 ± 0.7	7.5 ± 0.8
	12_1–11_1 (−1)	221387.23310	340.86708	614.69293	0.4 ± 0.1	-0.1 ± 0.9	6.4 ± 0.6
	12_0–11_0 (1)	221394.05650	343.21342	594.25027	0.4 ± 0.1	0.1 ± 0.8	7.2 ± 0.7
	12_3–11_3 (1)	221403.51080	321.83741	618.57225	0.3 ± 0.1	-0.3 ± 1.0	6.0 ± 0.8
	12_2–11_2 (1)	221422.34250	333.71483	596.20046	$*$	$*$	$*$
	12_1–11_1 (1)	221625.82810	340.89781	588.15547	0.4 ± 0.1	-0.6 ± 0.6	2.9 ± 0.4
$^{13}CH_3CN$	13_6–12_6	232077.26510	676.10972	335.52555	0.2 ± 0.1	-1.2 ± 1.0	3.4 ± 2.2
	13_5–12_5	232125.17430	366.00517	256.88144	0.3 ± 0.2	-1.2 ± 0.6	1.0 ± 2.5
	13_4–12_4	232164.39860	388.82528	192.51181	0.4 ± 0.1	0.0 ± 0.7	5.0 ± 1.7
	13_3–12_3	232194.92260	813.28078	142.43146	0.7 ± 0.1	-0.3 ± 0.4	3.6 ± 0.8
	13_2–12_2	232216.73400	419.33542	106.65163	0.5 ± 0.1	-0.3 ± 0.5	4.1 ± 1.2
	13_1–12_1	232229.82430	427.00159	85.18050	$*$	$*$	$*$
	13_0–12_0	232234.18830	429.58710	78.02284	$*$	$*$	$*$
CH_3CH_2CN	$25_{2,24}$–$24_{2,23}$	220660.91560	367.59999	143.01858	1.2 ± 0.1	-1.1 ± 0.2	5.1 ± 0.6
	$26_{1,25}$–$25_{1,24}$	231310.42000	383.10930	153.42092	1.7 ± 0.2	-1.3 ± 0.2	3.8 ± 0.4
	$27_{1,27}$–$26_{1,26}$	231854.21250	399.21212	157.73109	1.3 ± 0.1	-0.7 ± 0.2	4.6 ± 0.6
	$27_{0,27}$–$26_{0,26}$	231990.40940	399.25583	157.70511	$*$	$*$	$*$
CH_2CHCN	$24_{1,24}$–$23_{1,23}$	220561.39430	1045.66673	134.89930	0.5 ± 0.1	-1.0 ± 0.5	4.8 ± 1.4
	$23_{1,22}$–$22_{1,21}$	221123.85630	1001.46388	130.18397	0.3 ± 0.1	-0.7 ± 0.9	6.0 ± 2.2
	$24_{0,24}$–$23_{0,23}$	221766.03500	1046.14507	134.46535	0.5 ± 0.1	-0.6 ± 0.5	4.8 ± 1.2
	$23_{2,21}$–$22_{2,20}$	222153.49590	996.92904	135.71020	$*$	$*$	$*$
	$24_{1,23}$–$23_{1,22}$	230487.93630	1044.95160	141.24559	0.4 ± 0.2	-1.9 ± 0.7	2.7 ± 2.8
	$25_{0,25}$–$24_{0,24}$	230738.55760	1089.83000	145.53896	0.6 ± 0.2	-0.6 ± 0.4	2.4 ± 0.9
	$24_{2,22}$–$23_{2,21}$	231952.33100	1040.74852	146.84218	0.6 ± 0.1	-1.6 ± 0.4	2.4 ± 0.7
HNCO	$10_{1,9}$–$9_{1,8}$	220585.20000	27.83031	101.50215	1.1 ± 0.2	-0.2 ± 0.3	5.0 ± 0.8
CH_3OH	10_2–$9_3\ A-$	231281.15000	2.67310	165.34719	1.9 ± 0.2	-1.2 ± 0.2	5.0 ± 0.5
	22_4–$21_5\ E$	230368.19900	6.59478	682.74214	$*$	$*$	$*$
$^{13}CH_3OH$	$8_{1,8}$–$7_{0,7}\ A-$	221285.24100	5.01418	87.11782	0.5 ± 0.1	-1.0 ± 0.7	7.1 ± 1.7

Table 1 — *Continued.*

Molecule	Quantum Numbers	Frequency (MHz)	$S_{ij}\mu^2$ (debye^2)	E_u (K)	I (Jy beam^{-1})	Velocity (km s^{-1})	FWHM (km s^{-1})
(1)	(2)	(3)	(4)	(5)	(6)	(7)	(8)
CH_3OCHO	$18_{14,4}$–$17_{14,3}$ E	220815.20400	4.77300	105.85683	×	×	×
	$18_{15,3}$–$17_{15,2}$ A	220977.94900	14.81100	250.09976	0.5 ± 0.2	-1.2 ± 0.4	2.4 ± 0.9
	$18_{14,4}$–$17_{14,3}$ E	221049.88400	19.11600	230.86975	0.2 ± 0.1	-0.6 ± 1.4	7.1 ± 3.8
	$18_{13,5}$–$17_{13,4}$ A	221141.07100	23.11000	212.97153	0.3 ± 0.1	-0.9 ± 0.9	6.8 ± 2.2
	$18_{13,6}$–$17_{13,5}$ E	221158.47200	23.10900	212.95798	0.3 ± 0.3	-1.5 ± 0.5	1.6 ± 1.8
	$18_{12,6}$–$17_{12,5}$ E	221260.63000	26.79700	196.40266	0.1 ± 0.2	0.2 ± 1.6	2.6 ± 3.7
	$18_{12,7}$–$17_{11,6}$ A	221265.63600	26.79600	196.40002	*	*	*
	$18_{12,7}$–$17_{12,6}$ E	221280.83400	26.79500	196.38780	0.2 ± 0.1	-0.7 ± 1.2	2.7 ± 2.6
	$18_{11,7}$–$17_{11,6}$ E	221424.50300	30.17900	181.16821	*	*	*
	$18_{11,7}$–$17_{11,6}$ A	221432.98700	30.17700	181.16430	0.4 ± 0.1	-1.2 ± 0.7	3.6 ± 1.3
	$18_{11,8}$–$17_{11,7}$ E	221445.56100	30.17700	181.15339	0.3 ± 0.1	-1.2 ± 1.0	4.7 ± 2.1
	$18_{10,8}$–$17_{10,7}$ E	221649.27300	33.25800	167.27329	0.2 ± 1.2	-1.5 ± 1.2	4.0 ± 2.9
	$18_{10,9}$–$17_{10,8}$ A	221661.09300	33.25600	167.26667	0.8 ± 0.1	-1.2 ± 0.3	4.8 ± 0.8
	$18_{4,15}$–$17_{4,14}$ A	221674.67500	45.22200	112.05313	0.4 ± 0.1	-0.0 ± 0.7	6.7 ± 1.7
	$18_{9,9}$–$17_{9,8}$ A	221979.39900	36.03400	154.71574	0.3 ± 0.1	-2.4 ± 1.4	10.7 ± 4.0
	$18_{9,10}$–$17_{9,9}$ E	221985.63300	36.03500	154.71028	0.4 ± 0.1	-1.4 ± 0.9	6.0 ± 1.8
CH_3OCH_3	$24_{4,20}$–$23_{5,19}$ EE	220847.66600	99.56950	297.49662	0.1 ± 0.1	-2.4 ± 2.3	6.0 ± 5.4
	$23_{4,20}$–$23_{3,21}$ EE	220893.41500	340.17998	274.43535	0.5 ± 0.1	-0.9 ± 0.5	5.6 ± 1.3
	$27_{5,22}$–$27_{4,23}$ EE	221197.21400	457.47876	380.58782	*	*	*
	$21_{2,20}$–$21_{1,21}$ EE	222032.94600	135.26372	213.34669	0.3 ± 0.1	-1.3 ± 1.0	6.3 ± 2.1
	$4_{3,2}$–$3_{2,1}$ EA	222238.87700	9.89321	21.75719	0.4 ± 0.2	-1.9 ± 0.5	1.6 ± 1.0
	$4_{3,2}$–$3_{2,1}$ EE	222247.61100	48.00818	21.75761	1.0 ± 0.1	-1.4 ± 0.3	4.2 ± 0.6
	$4_{3,2}$–$3_{2,1}$ AA	222254.59700	43.82102	21.75651	0.7 ± 0.1	-2.3 ± 0.4	4.4 ± 0.8
	$4_{3,1}$–$3_{2,1}$ EE	222258.71100	22.07834	21.75670	0.6 ± 0.1	-0.8 ± 0.8	3.9 ± 1.0
	$28_{5,23}$–$27_{6,22}$ EE	230367.55300	113.80922	406.35321	*	*	*
	$10_{7,3}$–$11_{8,4}$ AE	230478.95300	2.82786	140.00103	×	×	×
	$13_{0,13}$–$12_{1,12}$ EE	231987.85800	271.84007	80.92307	*	*	*
CH_2CO	$11_{4,7}$–$10_{4,6}$	222119.92150	19.08471	275.19303	×	×	×
	$11_{3,9}$–$10_{3,8}$	222200.67600	61.08400	182.25648	1.3 ± 0.1	0.2 ± 0.3	6.7 ± 0.8
	$11_{2,10}$–$10_{2,9}$	222228.58700	21.51052	116.12409	0.3 ± 0.1	-2.4 ± 0.8	6.1 ± 2.2
SO_2	$11_{1,11}$–$10_{0,10}$	221965.21960	20.56551	60.36133	8.8 ± 0.4	-1.1 ± 0.1	5.8 ± 0.3
^{33}SO	$11_{1,11}$–$10_{0,10}$, F=25/2–23/2	220617.77850	23.09066	61.09988	*	*	*
	$14_{3,11}$–$14_{2,12}$, F=31/2–31/2	220985.77930	25.14909	120.26239	0.4 ± 0.1	-0.3 ± 0.3	1.6 ± 0.9
	$14_{3,11}$–$14_{2,12}$, F=27/2–27/2	220988.67530	21.76760	120.26224	0.2 ± 0.2	-1.1 ± 0.7	2.0 ± 1.7
^{34}SO	$22_{2,20}$–$22_{1,21}$	221114.89710	33.77375	248.19030	0.9 ± 0.1	-0.2 ± 0.3	4.3 ± 0.7
	$13_{2,12}$–$13_{1,13}$	221735.71460	13.03340	92.58307	1.3 ± 0.1	-0.5 ± 0.2	4.1 ± 0.5
OCS	19–18	231060.99340	9.71907	110.89923	8.3 ± 0.5	-1.7 ± 0.1	5.3 ± 0.3
$O^{13}CS$	19–18	230317.50000	9.72143	110.54285	1.3 ± 0.1	-0.7 ± 0.3	5.6 ± 0.6
^{13}CS	5–4	231220.68520	38.33376	33.29137	11.7 ± 1.2	-2.3 ± 0.3	5.5 ± 0.7
CH_3CCH	13_5–12_5	222061.03200	6.74610	253.07964	0.4 ± 0.1	-0.5 ± 0.8	5.0 ± 1.8
	13_4–12_4	222099.15000	7.16773	188.84188	0.9 ± 0.1	-2.2 ± 0.4	5.9 ± 0.9
	13_3–12_3	222128.80800	13.84590	139.43556	2.9 ± 0.3	-2.1 ± 0.3	5.1 ± 0.7
	13_2–12_2	222150.00800	7.72992	103.19011	*	*	*
	13_1–12_1	222162.72900	7.87048	81.77753	*	*	*
	13_0–12_0	222166.96900	7.91731	74.64000	*	*	*
t-HCOOH	$10_{1,9}$–$9_{1,8}$	231505.60760	19.98560	64.46633	0.4 ± 0.1	-1.0 ± 0.5	2.9 ± 1.2
Hα	H30α	231900.92800	0.0	0.0	5.6 ± 0.2	0.1 ± 0.4	28.5 ± 0.9
Hβ	H38β	222011.75500	0.0	0.0	1.6 ± 0.1	-0.9 ± 0.6	29.1 ± 1.4

Notes: * indicates that the different transitions are blended with each other and × indicates the signal-to-noise ratio of the spectrum is too low to produce a satisfactory fit.

Table 2 The Physical Parameters

Molecule	$T_{\rm rot}$ (K)	N ($\rm cm^{-2}$)	$f_{\rm H_2}$	θ ($''$)
(1)	(2)	(3)	(4)	(5)
CH_3CN	156 ± 10	$(3.1 \pm 1.3) \times 10^{15}$	$(2.4 \pm 1.0) \times 10^{-9}$	2.93
$CH_3{}^{13}CN$	156 ± 10	$(3.0 \pm 2.0) \times 10^{14}$	$(3.0 \pm 1.5) \times 10^{-10}$	2.93
$^{13}CH_3CN$	156 ± 10	$(2.0 \pm 0.5) \times 10^{14}$	$(1.1 \pm 0.4) \times 10^{-10}$	2.93
$CH_3CN_{v8=1}$	165 ± 23	$(5.6 \pm 0.3) \times 10^{15}$	$(4.3 \pm 0.2) \times 10^{-9}$	···
CH_3CH_2CN	171 ± 9	$(1.2 \pm 0.8) \times 10^{15}$	$(9.5 \pm 6.0) \times 10^{-10}$	···
CH_2CHCN	178 ± 42	$(4.8 \pm 2.7) \times 10^{14}$	$(3.7 \pm 2.1) \times 10^{-10}$	···
CH_3OCHO	121 ± 71	$(1.4 \pm 0.1) \times 10^{16}$	$(1.1 \pm 0.1) \times 10^{-8}$	···
CH_3OCH_3	129 ± 17	$(1.2 \pm 0.3) \times 10^{17}$	$(9.6 \pm 2.3) \times 10^{-8}$	1.39
CH_2CO	96 ± 15	$(2.3 \pm 1.1) \times 10^{15}$	$(1.8 \pm 0.8) \times 10^{-9}$	2.98
CH_3CCH	99 ± 34	$(7.8 \pm 0.1) \times 10^{15}$	$(6.0 \pm 0.1) \times 10^{-9}$	10.05
HNCO	160	2.6×10^{15}	2.0×10^{-9}	···
CH_3OH	121	1.5×10^{17}	1.2×10^{-7}	2.13
$^{13}CH_3OH$	121	1.4×10^{16}	1.1×10^{-8}	2.13
SO_2	165	3.7×10^{17}	2.8×10^{-7}	1.39
$^{33}SO_2$	165	3.4×10^{15}	2.6×10^{-9}	1.39
$^{34}SO_2$	165	2.4×10^{16}	1.8×10^{-8}	1.39
OCS	120	1.6×10^{16}	1.2×10^{-8}	3.72
$O^{13}CS$	120	2.1×10^{15}	1.6×10^{-9}	3.72
^{13}CS	75	5.7×10^{14}	4.4×10^{-10}	8.74
t-HCOOH	120	7.2×10^{14}	5.5×10^{-10}	2.85

Notes: Column (5) gives the deconvolved source size of the circular Gaussian component. Non-isotopic and isotopic molecules adopt the same source size. Some molecular lines are compact and unresolved.

gas manifest the immediate physical and chemical environment of the star-forming cores. Under the assumption of LTE, the physical parameters can be acquired through solving the radiative transfer equation by using XCLASS, including the source size, line profile, line blending, beam filling factor, background temperature, excitation and opacity. The fitting functions and modeling processes were described in detail in Möller et al. (2017).

For each kind of molecule, we chose the unblended and stronger emission line to measure the source size by two dimensional Gaussian fitting of the line emission region, which are shown in the moment 0 images in Figure 3. The line profile and line width were derived from the line spectrum fitting in Figure 2. The line blending, beam dilution and line opacity were taken into account in the calculations (Möller et al. 2017). The MAGIX package was used to obtain an optimal fitting solution for molecules with more than three transitions. By using different algorithms, MAGIX derives the parameter space and reduces the χ^2 to a minimum level (Möller et al. 2013). Combining XCLASS and MAGIX can estimate the most reasonable simulation parameters. For molecules with fewer than three transitions, we fixed their rotational temperature to that derived from the chemically related molecular species to estimate their column density. All the parameters are presented in Table 2.

The derived rotational temperatures for nitrogen-bearing molecules range from 156±10 to 178±42 K (see Column (2) of Table 2), which are slightly higher than those of oxygen-bearing molecules ranging from 96±15 to 129±17 K. Rotational temperature difference has been observed in other SFRs, e.g., G19.61−0.23 (Qin et al. 2010) in which the temperatures of N-bearing molecules (290–609 K) are much higher than those of O-bearing molecules (95–151 K). The line emission peaks of the oxygen-bearing and nitrogen-bearing molecules in G19.61−0.23 are different, suggesting a different chemical environment between oxygen- and nitrogen-bearing molecules. On the other hand, similar gas temperatures and distributions have been found between nitrogen- and oxygen-bearing molecules in W51 North, indicating that these molecules are well mixed and originate from the same physical environments (Rong et al. 2016). Although there is a slight difference between

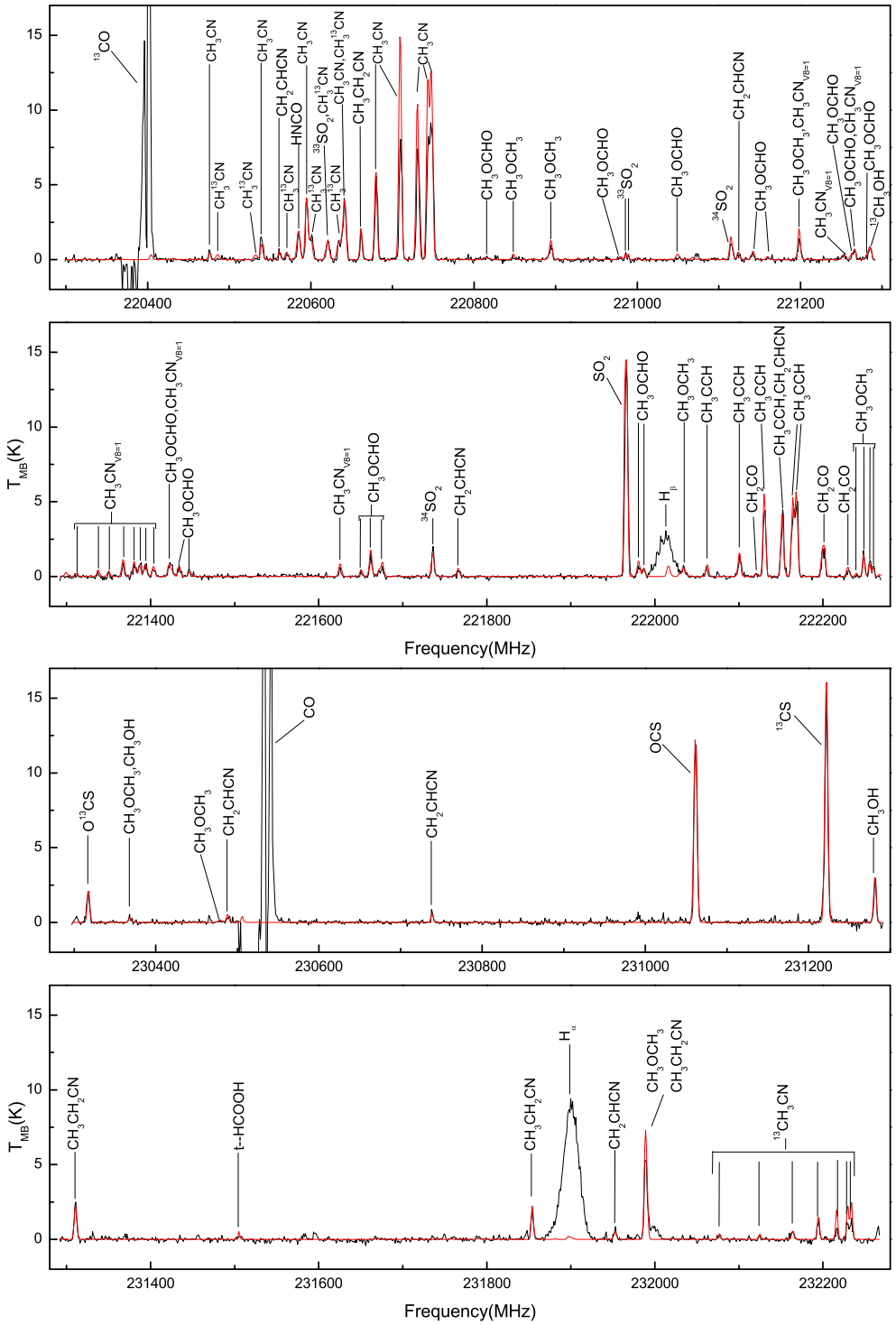

Fig. 2 The LSB and USB spectra extracted at the position of the 1.3 mm continuum peak. *Black curves* are the observed spectra and *red curves* are the simulated spectra. The corresponding molecule names are marked.

the rotational temperature of nitrogen-bearing molecules and oxygen-bearing molecules in G10.6−0.4, considering the same spatial distribution of these molecules in G10.6−0.4, we argue that the oxygen- and nitrogen-bearing molecules are mixed in the star forming core of G10.6−0.4. The lowest temperature of nitrogen-bearing molecule CH_3CN is 156±10 K obtained from our calculations, which is consistent with the previous result

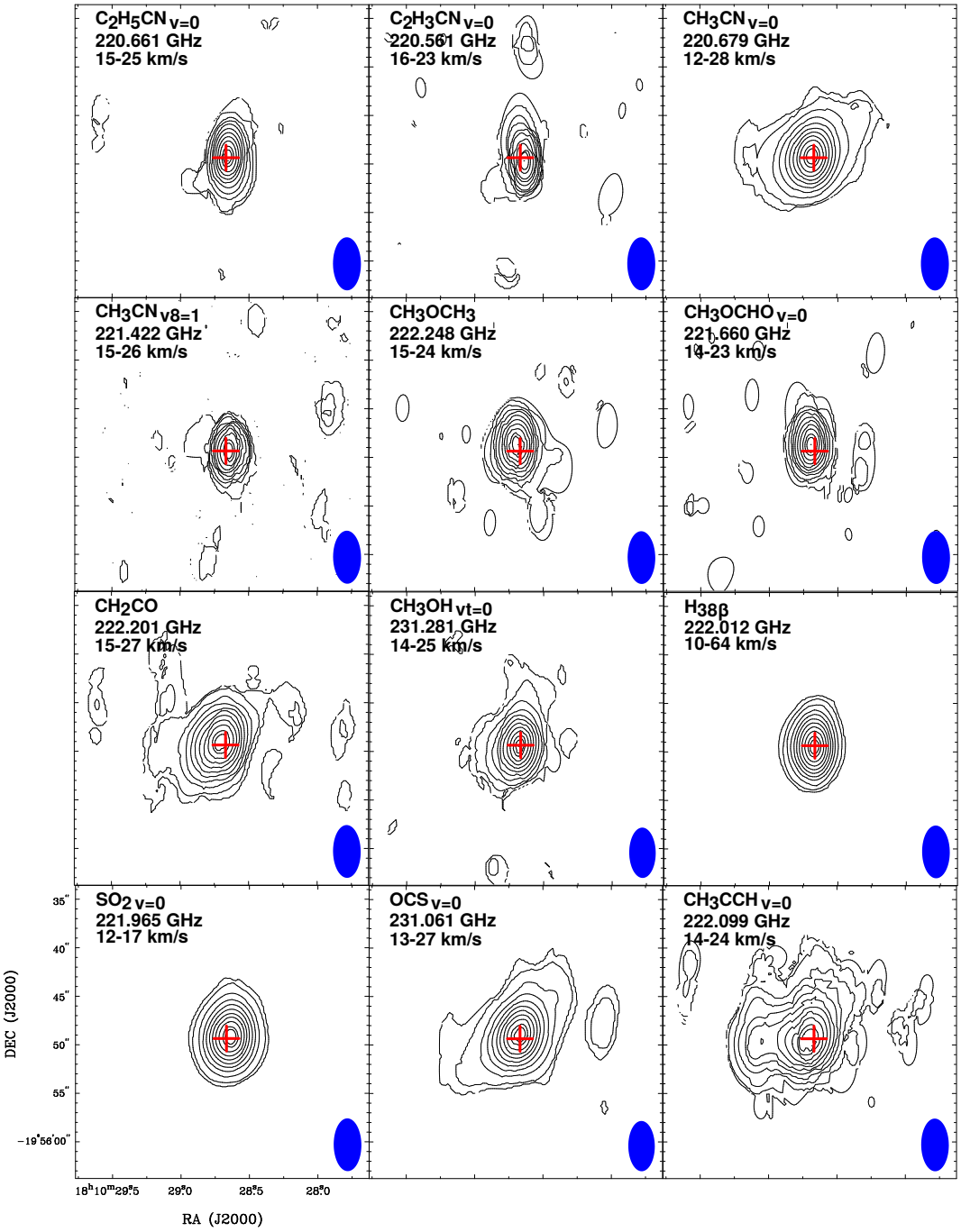

Fig. 3 Velocity-integrated intensity (moment 0) images of 12 selected molecular lines. In each panel, contours are 5, 10, 15, 20, 30, 40, 50, 60, 70, 80, 90 and 100 per cent of the peak intensity. The peak values of CH_3CH_2CN, CH_2CHCN, CH_3CN, $CH_3CN_{v8=1}$, CH_3OCH_3, CH_3OCHO, CH_2CO, CH_3OH, $H38_\beta$, SO_2, OCS and CH_3CCH are 5.9, 2.3, 28.2, 3.9, 3.7, 2.1, 8.8, 9.6, 50.6, 54.6, 41.2 and 14.3 Jy beam^{-1} km s^{-1}, respectively. The synthesized beam is visible in the bottom-right corner with a *solid blue ellipse* and a *cross symbol* marks the peak position derived from the 1.3 mm continuum image.

($T_{\rm rot}$ = 160 K) obtained by Liu et al. (2013). Sulphur-bearing molecules have a broader range of gas temperature, from 75 K (CS) to 165 K (SO_2), indicating these molecules probe different spatial distributions and dynamic conditions. For instance, SO_2 shows a central concentration, and CS and OCS display extended emission to the northwest and southeast, probably tracing the outflows.

The column densities including 20 molecular species and their isotopologues are derived using the XCLASS package and are listed in column 3 of Table 2. The column density ranges of nitrogen-bearing molecules and oxygen-bearing molecules are from 2.0×10^{14} to 5.6×10^{15} cm^{-2} and from 2.3×10^{15} to 1.5×10^{17} cm^{-2}, respectively; the higher column density of oxygen-bearing molecules implies that the hot core is in the state of being O-rich. The column density of sulphur-bearing molecules is in the range of $5.7\times10^{14} - 3.7\times10^{17}$ cm^{-2}.

The ratios of column densities of the identifiable molecules to the column density of the hydrogen molecule give fractional abundances ($f_{\rm H_2} = N_T/N_{\rm H_2}$) which are listed in column 4 of Table 2. The abundances for the oxygen-bearing molecules are from 5.5×10^{-10} to 1.2×10^{-7} and from 1.1×10^{-10} to 4.3×10^{-9} for nitrogen-bearing molecules. The oxygen-bearing molecules have higher abundances but lower rotational temperatures than nitrogen-bearing molecules. The same results are inferred in other MSFRs (e.g., Blake et al. 1987; Wyrowski et al. 1999; Qin et al. 2010; Rong et al. 2016). In addition, the abundances of sulphur-bearing molecules are inferred to be in the range from 4.4×10^{-10} to 2.8×10^{-7}.

The chemical evolution models of massive star formation (e.g., Rodgers & Charnley 2001) suggest that O-rich cores form first, then become N-rich as the molecular cores evolve and the temperature rises. The observational results, such as the higher temperature, column density and abundance of O-bearing molecules, compared to N-bearing molecules and the co-spatial distribution of these two classes of molecules, invoke a scenario that the hot core in G10.6−0.4 is in an early transitional phase from being O-rich to N-rich.

4 DISCUSSION

4.1 Comments on Individual Molecule Classes

4.1.1 Nitrogen-bearing molecules

Methyl cyanide (CH_3CN) is commonly used to trace a hot core environment (e.g., Remijan et al. 2004). CH_3CN is an in-situ synthesized molecule, which is produced by radiative association of CN with CH_3, and of CH_3^+ with HCN by the ion−molecule reaction (Charnley et al. 1992). Rotational and vibrational transitions of CH_3CN and its isotopes were detected in our observations, namely CH_3CN, $CH_3CN_{v8=1}$, $CH_3{}^{13}CN$ and $^{13}CH_3CN$. Nine rotational transitions (J = 12–11) of CH_3CN with upper-level energies of 69–526 K were detected, and the derived rotational temperature and fractional abundance are 156 ± 10 K and $(2.4 \pm 1.0) \times 10^{-9}$, respectively. Derived rotational temperature of 156 K suggested that different K ladders of CH_3CN are thermalized and can be characterized by a single temperature. Thirteen vibrationally excited $CH_3CN_{v8=1}$ transitions with upper-level energies of 588–850 K were observed. The rotational temperature and abundance are 165 ± 23 K and $(4.3 \pm 0.2) \times 10^{-9}$, respectively. Usually vibrationally excited CH_3CN lines require higher excited conditions than those of rotational transitions and trace inner parts of the cloud. Therefore, one expects to see that $CH_3CN_{v8=1}$ lines have higher gas temperature at the center of the hot core if the source is internally heated. In case of G10.6−0.4, emission peaks of the molecular lines are consistent with those of the UC HII region, indicating that gas is probably heated by the central massive star. Higher gas temperature and fractional abundance indicate that $CH_3CN_{v8=1}$ is denser than CH_3CN and closer to embedded OB stars. Multiple $CH_3{}^{13}CN$ and $^{13}CH_3CN$ transitions are observed. The inferred $^{12}C/^{13}C$ ratio of 10 is consistent with extrapolation from the isotopologue ratio gradient of $^{12}C/^{13}C$ (Wilson & Rood 1994).

Vinyl cyanide (CH_2CHCN) and ethyl cyanide (CH_3CH_2CN) are widely distributed in MSFRs, and are generally found in hot cores (e.g. Sakai et al. 2018; Widicus Weaver et al. 2017; Fu & Lin 2016). Seven transitions of CH_2CHCN with upper-level energies of 130–147 K were detected, and a rotational temperature of 178±42 K and abundance of $(3.7 \pm 2.1) \times 10^{-10}$ are derived. Four transitions of CH_3CH_2CN with the upper-level energies of 143–158 K were detected, and a rotational temperature of 171±9 K and abundance of $(9.5 \pm 6.0) \times 10^{-10}$ are derived. The abundance ratio in G10.6−0.4 (R=$N_{\rm CH_2CHCN}/N_{\rm CH_3CH_2CN}$) is about 0.4, which is consistent with the statistical results of MSFRs (Fontani et al. 2007) and the hot core's age is estimated to be about (4.5–5.5)×10^4 yr.

4.1.2 Oxygen-bearing molecules

Dimethyl ether (CH_3OCH_3) has two methyl groups. It produces a large amplitude vibration along the CO-bond and thus shows an asymmetric top. CH_3OCH_3 has been often observed in MSFRs. Eleven transitions of CH_3OCH_3 with upper-level energies of 22–406 K were detected from our data. A rotational temperature of

129 ± 17 K and abundance of $(9.6 \pm 2.3) \times 10^{-8}$ are derived. Methyl formate (CH_3OCHO) is a large oxygen-bearing molecule, and is often found in hot cores and corinos in other star-forming regions (Blake et al. 1987; Hatchell et al. 1998; Cazaux et al. 2003). Sixteen transitions of CH_3OCHO with upper-level energies of 106–250 K were detected, and a rotational temperature of 121 ± 71 K and abundance of $(1.1 \pm 0.1) \times 10^{-8}$ are derived. Previous observations have shown that the abundance ratio of CH_3OCH_3 to CH_3OCHO is in the range of 3.5–9 (Brouillet et al. 2013). Our observations derived a ratio ∼8.7. The moment 0 images show similar gas distributions, and the simulated values of rotational temperatures and abundances are also very close for CH_3OCH_3 and CH_3OCHO. A large number of previous observations have shown that the similarity between the two molecules is not an accidental result (e.g., Brouillet et al. 2013; Rong et al. 2016). Therefore, these pieces of observational evidence support that the similarity for two molecules is chemically related in the hot core of G10.6−0.4. The pure gas-phase ion-molecule chemistry model shows that the ion-molecule reactions of $CH_3OH_3^+$ with H_2CO and CH_3OH are the formation paths to generate the methyl formate and dimethyl ether (e.g., Blake et al. 1987; Taquet et al. 2016). However, Garrod et al. (2008) argue that the two molecules are generated from the grain surface directly and evaporate into the gas phase after the increase of environmental temperature. The gas phase model indicates that abundance of the two molecules remains similar with the evolution (Charnley et al. 1995), while simulation of the grain surface model has a distinct difference (Model M) or a sharp decline (Model F) (Garrod et al. 2008). Our result suggests that these two molecular species may be formed in the gas-phase model.

Ketene (CH_2CO) has the simplest structure among ketene type molecules and was first observed in cold dark clouds (Ohishi et al. 1991). Three transitions of CH_2CO with upper-level energies of 116–275 K were detected, and a rotational temperature of 96 ± 15 K and abundance of $(1.8 \pm 0.8) \times 10^{-9}$ are derived. The derived low rotational temperature (Bisschop et al. 2007) favors that the CH_2CO molecule is formed on the grain surface and evaporates to the gas phase (Garrod et al. 2008).

4.1.3 Sulfur-bearing molecules

Sulfur-bearing molecules are often used to trace the outflow, shock and hot toroid in SFRs. One transition of SO_2, three transitions of $^{33}SO_2$ and two transitions of $^{34}SO_2$ with upper-level energies of 60, 61–120 and 93–248 K are detected, respectively. Both the SO_2 and its isotopologues have the same rotational temperatures of 165 K. The abundances of SO_2, $^{33}SO_2$ and $^{34}SO_2$ are 2.8×10^{-7}, 2.6×10^{-9} and 1.8×10^{-8}, respectively. The abundance ratios, $SO_2/^{34}SO_2$ of 15.6 and $^{34}SO_2/^{33}SO_2$ of 7.0, are consistent with the $^{32}S/^{34}S$ and $^{34}S/^{33}S$ ratios in MSFRs for 3 kpc $\leq D_{\rm GC} \leq$9 kpc (Chin et al. 1996). Both OCS and $O^{13}CS$ have a single transition in the 230 GHz band. They have the same rotational temperature of 120 K and abundances of 1.2×10^{-8} and 1.6×10^{-9}, respectively. The formation path of OCS is the combination of carbon monoxide and sulfur atoms (Charnley 1997). Neutralization of HCS^+ and H_3CS^+ leads to formation of the carbon monosulfide CS molecule (Charnley 1997). One transition of ^{13}CS is detected. Assuming a rotational temperature of 75 K, the ^{13}CS abundance is estimated to be 4.4×10^{-10}.

4.1.4 Methyl acetylene (CH_3CCH)

Methyl acetylene (CH_3CCH) is a prolate symmetric top molecule and is thought to be a good probe of the kinetic temperature of dense molecular gas (e.g., Askne et al. 1984; Bergin et al. 1994). Six transitions of CH_3CCH with upper-level energies of 75–253 K were detected from the present data, and a rotational temperature of 99 ± 34 K and abundance of $6.0 \pm 0.1 \times 10^{-9}$ are derived. Single dish observations of CH_3CCH towards the W31 region (including G10.6−0.4) revealed a fractional abundance for CH_3CCH of 6.8×10^{-9} (Miettinen et al. 2006). The beams of those observations are similar to our observation; in addition, the CH_3CCH line was extracted from the peak position towards G10.6−0.4 in our case. This favors that the distribution of methyl acetylene is extended and uniform in G10.6−0.4, and beam dilution can be neglected. The high fractional abundance of CH_3CCH cannot be explained by the gas–phase model (e.g., Lee et al. 1996). Instead, the continuous hydrogenation reaction of C_3 is a possible route to generate CH_3CCH on the grain surface (Hickson et al. 2016) in G10.6−0.4.

4.2 Comparison with Other Hot Cores

G10.6−0.4 was detected with rich organic molecules from our observations. The detected nitrogen-bearing and oxygen-bearing molecules show similar gas distribution and rotational temperature, suggesting that these

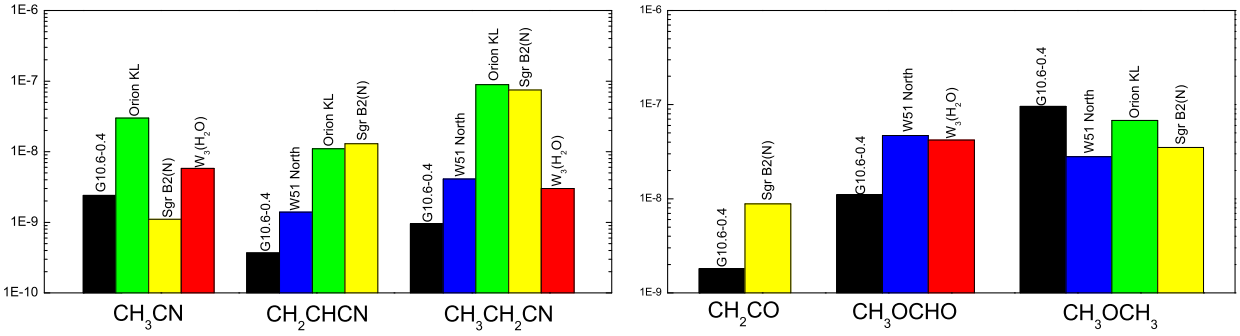

Fig. 4 The abundance of molecular species towards G10.6−0.4 relative to H_2 (*black bars*), compared to abundance towards W51 North (*blue bars*) from Rong et al. (2016), the Orion KL hot core (*green bars*) from Crockett et al. (2014)), the Sgr B2 (N) hot core (*yellow bars*) from Neill et al. (2014) and the W3(H_2O) hot core (*red bars*) from Qin et al. (2015).

molecular species may be formed in the same physical environments. By comparing the rotational temperatures and molecular abundances of G10.6−0.4 with other representative MSFRs, such as W51 North (Rong et al. 2016), W3(H_2O) (Qin et al. 2015), the Orion KL hot core (Crockett et al. 2014) and Sgr B2(N) (Neill et al. 2014), we can investigate the difference in physical and chemical environments among these hot cores. As these hot core studies employed the same methods (line survey of complex molecules with mm and submm telescopes) and analysis tools (physical parameters fit using XCLASS under the LTE assumption), such comparison is reasonable. The rotational temperature of nitrogen-, oxygen- and sulfur-bearing molecules for G10.6–0.4 ranges from 96 to 178 K, and is closest to that of W51 North (105–180 K). The molecular gas in the Orion KL hot core and Sgr B2(N) is much hotter, with rotational temperatures ranging from 150 to 300 K. Among these five hot cores, W3(H_2O) has the highest rotational temperature (∼360 K).

A comparison of molecular abundances for G10.6−0.4 with other hot cores is shown in Figure 4. The abundances of CH_2CHCN and CH_3CH_2CN in G10.6−0.4 are lower than those from the Orion KL hot core and Sgr B2(N), and also there are clearly differences in abundance of CH_3CN among G10.6−0.4, Orion KL hot core and Sgr B2(N).

Comparison of molecular rotational temperatures and abundances with other sources suggests that the envelope of G10.6−0.4 has different conditions from the Orion KL hot core, Sgr B2(N) and W3(H_2O), while G10.6−0.4 and W51 North seem to have similar physical and chemical conditions.

5 SUMMARY

We presented a molecular line survey observed with the SMA at 1.3 mm wavelength towards the MSFR G10.6−0.4, the most compact and brightest source in the W31 complex. A total of 99 transitions from 22 molecular species and their isotopologues were detected, including nitrogen-bearing molecules, oxygen-bearing molecules, sulfur-bearing molecules and two radio recombination lines. The main conclusions are summarized as follows:

(1) The velocity-integrated intensity images show that all molecular line emission is concentrated in the central core. The peaks of CH_3CH_2CN, CH_3CN, CH_3OH, OCS and radio recombination lines ($H30_\alpha$, $H38_\beta$) coincide with the continuum peak, while the peaks of CH_2CHCN, CH_3OCH_3, CH_3OCHO, CH_2CO, SO_2 and CH_3CCH slightly deviate from the continuum peak.
(2) The derived rotational temperatures of nitrogen-bearing molecules range from 156±10 to 178±42 K, and from 96±15 to 129±17 K for oxygen-bearing molecules. The similar gas temperatures and co-spatial distributions between nitrogen-bearing and oxygen-bearing molecules imply that the oxygen- and nitrogen-bearing molecules are well mixed and originate from the same physical environments.
(3) The abundance ratio CH_2CHCN/CH_3CH_2CN is about 0.4, which is consistent with the statistical re-

sults of MSFRs, and the hot core age is estimated to be about 5×10^4 yr. The observations support that CH_2CHCN is generated by gas-phase reactions related to CH_3CH_2CN, while CH_3CH_2CN could be synthesized on the grain surface.

(4) CH_3OCH_3 and CH_3OCHO have similar gas distributions, rotational temperatures and fractional abundances, suggesting the two molecular species in G10.6−0.4 are chemically related. Both molecules could be formed on the grain surface.

(5) G10.6−0.4 and W51 North have similar molecular rotational temperatures and abundances, whereas the hot cores in W3(H_2O), the Orion KL hot core and Sgr B2(N) are much hotter. The similar physical and chemical properties between G10.6−0.4 and W51 North indicate that the environments of the two MSFRs are similar.

Acknowledgements TA thanks grant support by the Youth Innovation Promotion Association of CAS and we appreciate Dr. Sheng-Li Qin's helpful discussion. The Submillimeter Array is a joint project between the Smithsonian Astrophysical Observatory and the Academia Sinica Institute of Astronomy and Astrophysics and is funded by the Smithsonian Institution and Academia Sinica.

References

Askne, J., Hoglund, B., Hjalmarson, A., & Irvine, W. M. 1984, A&A, 130, 311
Bergin, E. A., Goldsmith, P. F., Snell, R. L., & Ungerechts, H. 1994, ApJ, 431, 674
Bisschop, S. E., Jørgensen, J. K., van Dishoeck, E. F., & de Wachter, E. B. M. 2007, A&A, 465, 913
Blake, G. A., Sutton, E. C., Masson, C. R., & Phillips, T. G. 1987, ApJ, 315, 621
Brouillet, N., Despois, D., Baudry, A., et al. 2013, A&A, 550, A46
Caswell, J. L., Murray, J. D., Roger, R. S., Cole, D. J., & Cooke, D. J. 1975, A&A, 45, 239
Cazaux, S., Tielens, A. G. G. M., Ceccarelli, C., et al. 2003, ApJ, 593, L51
Charnley, S. B., Tielens, A. G. G. M., & Millar, T. J. 1992, ApJ, 399, L71
Charnley, S. B., Kress, M. E., Tielens, A. G. G. M., & Millar, T. J. 1995, ApJ, 448, 232
Charnley, S. B. 1997, ApJ, 481, 396
Chin, Y.-N., Henkel, C., Whiteoak, J. B., Langer, N., & Churchwell, E. B. 1996, A&A, 305, 960
Crockett, N. R., Bergin, E. A., Neill, J. L., et al. 2014, ApJ, 787, 112
Downes, D., Wilson, T. L., Bieging, J., & Wink, J. 1980, A&AS, 40, 379
Evans, II, N. J. 1999, ARA&A, 37, 311
Fish, V. L., Reid, M. J., Argon, A. L., & Zheng, X.-W. 2005, ApJS, 160, 220
Fontani, F., Pascucci, I., Caselli, P., et al. 2007, A&A, 470, 639
Fu, L., & Lin, G.-M. 2016, RAA (Research in Astronomy and Astrophysics), 16, 182
Garrod, R. T., Widicus Weaver, S. L., & Herbst, E. 2008, ApJ, 682, 283
Goss, W. M., & Shaver, P. A. 1970, Australian Journal of Physics Astrophysical Supplement, 14, 1
Habing, H. J., Goss, W. M., Matthews, H. E., & Winnberg, A. 1974, A&A, 35, 1
Hatchell, J., Thompson, M. A., Millar, T. J., & MacDonald, G. H. 1998, A&AS, 133, 29
Herbst, E., & van Dishoeck, E. F. 2009, ARA&A, 47, 427
Hickson, K. M., Wakelam, V., & Loison, J.-C. 2016, Molecular Astrophysics, 3, 1
Ho, P. T. P., & Haschick, A. D. 1981, ApJ, 248, 622
Ho, P. T. P., & Haschick, A. D. 1986, ApJ, 304, 501
Ho, P. T. P., Moran, J. M., & Lo, K. Y. 2004, ApJ, 616, L1
Keto, E. 2002, ApJ, 568, 754
Keto, E. R., Ho, P. T. P., & Haschick, A. D. 1987, ApJ, 318, 712
Keto, E. R., Ho, P. T. P., & Haschick, A. D. 1988, ApJ, 324, 920
Klaassen, P. D., Wilson, C. D., Keto, E. R., & Zhang, Q. 2009, ApJ, 703, 1308
Lee, H.-H., Bettens, R. P. A., & Herbst, E. 1996, A&AS, 119, 111
Lis, D. C., Carlstrom, J. E., & Keene, J. 1991, ApJ, 380, 429
Liu, H. B., Ho, P. T. P., Zhang, Q., et al. 2010, ApJ, 722, 262
Liu, H. B., Ho, P. T. P., & Zhang, Q. 2010, ApJ, 725, 2190
Liu, H. B., Zhang, Q., & Ho, P. T. P. 2011, ApJ, 729, 100
Liu, T., Wu, Y., Wu, J., Qin, S.-L., & Zhang, H. 2013, MNRAS, 436, 1335
Miettinen, O., Harju, J., Haikala, L. K., & Pomrén, C. 2006, A&A, 460, 721
Möller, T., Bernst, I., Panoglou, D., et al. 2013, A&A, 549, A21
Möller, T., Endres, C., & Schilke, P. 2017, A&A, 598, A7
Müller, H. S. P., Schlöder, F., Stutzki, J., & Winnewisser, G. 2005, Journal of Molecular Structure, 742, 215
Neill, J. L., Bergin, E. A., Lis, D. C., et al. 2014, ApJ, 789, 8
Ohishi, M., Suzuki, H., Ishikawa, S.-I., et al. 1991, ApJ, 380, L39
Pickett, H. M., Poynter, R. L., Cohen, E. A., et al. 1998, J. Quant. Spec. Radiat. Transf., 60, 883
Qin, S.-L., Wu, Y., Huang, M., et al. 2010, ApJ, 711, 399
Qin, S.-L., Schilke, P., Wu, J., et al. 2015, ApJ, 803, 39
Remijan, A., Shiao, Y.-S., Friedel, D. N., Meier, D. S., &

Snyder, L. E. 2004, ApJ, 617, 384
Rodgers, S. D., & Charnley, S. B. 2001, ApJ, 546, 324
Rong, J., Qin, S.-L., Zapata, L. A., et al. 2016, MNRAS, 455, 1428
Sakai, T., Yanagida, T., Furuya, K., et al. 2018, ApJ, 857, 35
Sanna, A., Reid, M. J., Menten, K. M., et al. 2014, ApJ, 781, 108
Sollins, P. K., Zhang, Q., Keto, E., & Ho, P. T. P. 2005, ApJ, 624, L49
Taquet, V., Wirström, E. S., & Charnley, S. B. 2016, ApJ, 821, 46
Turner, B. E., & Rubin, R. H. 1971, ApJ, 170, L113
van Dishoeck, E. F., & Blake, G. A. 1998, ARA&A, 36, 317
Widicus Weaver, S. L., Laas, J. C., Zou, L., et al. 2017, ApJS, 232, 3
Wilson, T. L. 1974, A&A, 31, 83
Wilson, T. L., & Rood, R. 1994, ARA&A, 32, 191
Wright, E. L., Fazio, G. G., & Low, F. J. 1977, ApJ, 217, 724
Wyrowski, F., Schilke, P., Walmsley, C. M., & Menten, K. M. 1999, ApJ, 514, L43
Zinnecker, H., & Yorke, H. W. 2007, ARA&A, 45, 481